

Article

Magnetron-Sputtered Long-Term Superhydrophilic Thin Films for Use in Solid-State Cooling Devices

Maria Barrera ^{*} , Olaf Zywitzki, Thomas Modes and Fred Fietzke

Fraunhofer-Institute for Electron Beam and Plasma Technology (FEP), Winterbergstraße 28, 01277 Dresden, Germany; olaf.zywitzki@fep.fraunhofer.de (O.Z.); thomas.modes@fep.fraunhofer.de (T.M.); fred.fietzke@fep.fraunhofer.de (F.F.)

* Correspondence: maria.isabel.barrera.marin@fep.fraunhofer.de

Abstract: Pulse-magnetron-sputtered long-term superhydrophilic coatings have been synthesized to functionalize the surfaces of solid-state cooling devices, e.g., electrocaloric heat pumps, where not only a complete wetting of the surface by a fluid is intended, but also fast wetting and dewetting processes are required. The coatings consist of a (Ti,Si)O₂ outer layer that provides lasting hydrophilicity thanks to the mesoporous structure, followed by an intermediate WO₃ film that enables the reactivation of the wettability through visible light irradiation, and a W underlayer which can work as a top electrode of the electrocaloric components thanks to its suitable electrical and thermal conductivity properties. Process parameter optimization for each layer of the stack as well as the influence of the microstructure and composition on the wetting properties are presented. Finally, water contact angle measurements, surface energy evaluations, and a contact line dynamics assessment of evaporating drops on the coatings demonstrate that their enhanced wetting performance is attributed not only to their intrinsic hydrophilic nature but also to their porous microstructure, which promotes wicking and spreading at the nanometric scale.

Keywords: pulsed magnetron sputtering; long-term superhydrophilicity; titanium dioxide; silicon dioxide; tungsten trioxide; tungsten; wetting; solid-state cooling



Citation: Barrera, M.; Zywitzki, O.; Modes, T.; Fietzke, F.

Magnetron-Sputtered Long-Term Superhydrophilic Thin Films for Use in Solid-State Cooling Devices.

Coatings **2024**, *14*, 622. <https://doi.org/10.3390/coatings14050622>

Academic Editor: Alberto Palmero

Received: 17 April 2024

Revised: 7 May 2024

Accepted: 13 May 2024

Published: 14 May 2024



Copyright: © 2024 by the authors. Licensee MDPI, Basel, Switzerland. This article is an open access article distributed under the terms and conditions of the Creative Commons Attribution (CC BY) license (<https://creativecommons.org/licenses/by/4.0/>).

1. Introduction

Global environmental regulations and market requirements have led to the need for heat generation sources with higher efficiency and a lower carbon footprint. Electrocaloric heat pumps are an emerging solid-state technology for cooling and heating applications and could replace compressor-based systems and harmful refrigerants. In this scenario, the heat transfer is carried out through latent heat when a fluid evaporates and/or condenses on the electrocaloric materials [1], meaning that their surface needs to be completely wetted by the working fluid for optimum heat transfer.

The wettability of a solid-state surface is influenced by its roughness, chemical composition, and surface free energy (SFE). The SFE of a solid surface provides a direct measure of intermolecular interactions at the interfaces, and typically a high value results in the formation of low water contact angles, thus leading to the improved wettability of the solid surface [2,3]. When a droplet is in contact with a smooth solid surface and at thermodynamic equilibrium, it forms an angle, θ_y , that can be expressed according to Young's equation:

$$\cos \theta_y = \frac{\gamma_{sv} - \gamma_{sl}}{\gamma_{lv}} \quad (1)$$

where γ_{sv} , γ_{sl} , and γ_{lv} are the solid–vapor, solid–liquid, and liquid–vapor interfacial tensions, respectively [4]. However, in the case of non-smooth surfaces, Wenzel's equation is used instead. It describes the effect of surface roughness on the contact angle:

$$\cos \theta_w = R \cos \theta_y \quad (2)$$

where R is a roughness factor, θ_w is the rough surface water contact angle, and θ_y is the characteristic water contact angle dependent on the interfacial energy between the three phases at the area of contact, i.e., Young's angle [5]. When a drop is deposited on a solid surface, the liquid either spreads completely and forms a film that covers the solid surface (complete wetting), or it spreads partially and forms a drop with a certain contact angle θ (partial wetting). Surfaces with $\theta > 90^\circ$ are commonly classified as hydrophobic, while those with contact angles smaller than 90° are known as hydrophilic. Moreover, if the contact angle remains below 10° , the surface is considered superhydrophilic or superwetting [6].

Coating the surface of materials with thin films has been one of the most widely used techniques for tuning their wettability, either by changing the chemical state of the surface or by adding roughness. Moreover, superhydrophilicity has been achieved by several authors, but only when the materials are freshly prepared and/or their surfaces are irradiated with ultraviolet (UV) light, as in the case of some metal oxide-containing coatings [7,8]. Their strong affinity to water is usually a short-lasting effect, which is altered by the accumulation of airborne contaminants on the surface and/or after storing the materials in a dark place.

Titanium dioxide (TiO_2) is a wide-band-gap semiconductor and one of the most extensively used photocatalysts. In the field of thin films, depending on the deposition conditions, it can exist in the crystalline forms anatase, rutile, or brookite, with anatase being highly photoactive. Due to its band gap energy of 3.2 eV and formation of oxygen vacancies, when irradiated with UV light, it exhibits photoinduced hydrophilicity and is thus commonly used for antifogging and self-cleaning applications [9–11]. Furthermore, some authors report an improvement in the stability and durability of the wetting properties of TiO_2 when combined with silicon dioxide (SiO_2), attributed to the characteristic mesoporous structure of the latter, which can increase the hydrophilicity even in the absence of light due to capillary effects [12–16].

Alternatively, tungsten trioxide (WO_3) is an n-type semiconductor that has several polymorphs depending on the formation temperature; monoclinic (17–330 °C), orthorhombic (330–740 °C), and tetragonal (>740 °C) are some of them [17,18]. Depending on the presence of oxygen vacancies in the crystal lattice and the different oxidation states, there are two forms of crystalline tungsten oxide, namely stoichiometric (WO_3) and non-stoichiometric (WO_{3-x}). Furthermore, the oxygen vacancies affect the growth behavior and band gaps of tungsten oxide thin films since they influence their structural arrangement. For example, amorphous WO_3 thin films have a wide band gap value of 3.4 eV, while crystalline films have a narrower band gap of approximately 2.7 eV [19]. Due to this wide variety of characteristics, tungsten oxide has been extensively investigated for gas sensing, electrochromic devices, photocatalysis, hydrophilicity, and optoelectronic applications [20].

In this work, we have developed pulse-magnetron-sputtered long-term superhydrophilic coatings that do not require activation by periodical UV exposure. They consist of a $(\text{Ti,Si})\text{O}_2/\text{WO}_3/\text{W}$ multilayer in which the enhanced wetting performance is attributed not only to their intrinsic hydrophilic chemistry but also to the porous microstructure that promotes capillary action and spreading at the nanometric scale. Process parameter optimization for each layer of the stack and the results on the influence of the microstructure and composition on the wetting properties for the desired application are presented in the next sections.

2. Materials and Methods

2.1. Thin Films Preparation

Deposition experiments were carried out by pulsed magnetron sputtering technology [21] using an industrial scale batch coating device with a volume of 1500 L, which has two dual magnetron systems with target dimensions $512 \times 128 \text{ mm}^2$, a hollow-cathode source for plasma pretreatment, and a unit for heating the substrates up to 700 °C. A

rotating substrate carrier was locked in front of magnetrons 3 and 4 in such a way that the substrates experienced a one-fold rotation in this central position at an average target distance of 100 mm (see Figure 1). Deposition parameters were varied until each coating of the multilayer was optimized for the required complete wetting application.

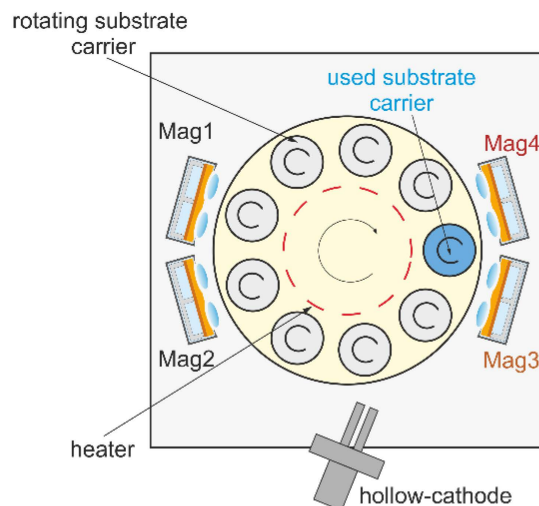


Figure 1. Schematic representation of the deposition arrangement.

Flat aluminum oxide ceramic (Al_2O_3 Rubalit[®] 710, A.L.L Lasertechnik, Munich, Germany), stainless steel (X5CrNi18-10, material No. 1.4301, Variolux GmbH, Arnsdorf, Germany), and borosilicate glass (Tempax, Siegert TFT GmbH, Hermsdorf, Germany) samples with dimensions $100 \times 60 \text{ mm}^2$ and a thickness of 0.63 mm, 0.95 mm, and 0.8 mm, respectively, were used as substrates.

Initially, the vacuum chamber was evacuated to $\sim 1 \times 10^{-3} \text{ Pa}$ and the substrates were heated to the desired temperature based on the coating to be deposited. Before thin-film deposition, the substrates were pre-treated with argon plasma for 5 min at a chamber pressure of 0.17 Pa.

Tungsten thin films were deposited by sputtering tungsten targets in Ar plasma using a double magnetron arrangement (magnetrons 3 and 4 in Figure 1); in this case, the substrate temperature and pulse lengths were varied (Table 1). For the tungsten trioxide coatings, the targets were reactively sputtered in a mixture of argon and oxygen gases at a fixed argon flow rate of 100 sccm and a total pressure of 1.8 Pa. The composition and stoichiometry of the coatings were tailored by controlling the oxygen flow using optical emission spectroscopy. For this purpose, the intensities of characteristic spectral lines of argon and oxygen were detected, their quotient was compared with a setpoint value, and the inlet of the reactive gas into the vacuum chamber was controlled depending on the result. Table 2 shows the deposition parameter variation for the tungsten trioxide thin films.

Table 1. Deposition parameters of W thin films and their measured electrical conductivity.

Sample	Temperature	Pulse Frequency	Voltage	Thickness	Rate	Electrical Conductivity
No.	°C	kHz	V	nm	nm/m	MS/m
W_1	250	2.5	645	5200	86	4.1
W_2	250	25	870	4600	76	3.1
W_3	500	2.5	654	5500	91	3.6
W_4	500	25	835	4800	80	3.4

Table 2. Deposition parameters of WO_x thin films.

Sample	Temperature	Setpoint	O ₂ Flow ¹	Total Pressure	Thickness	Rate
No.	°C	%	sccm	Pa	nm	nm/min
WO _x _1	250	70	145	1.21	2200	220
WO _x _2	250	90	140	1.28	2100	210
WO _x _3	250	130	120	1.40	1500	150
WO _x _4	250	130	120	1.40	1100	137
WO _x _5	500	130	190	1.80	1000	125

¹ Average value taken during the deposition process.

The titanium dioxide–silicon dioxide upper layer was synthesized by the co-sputtering of a titanium (on magnetron 4) and a silicon target (on magnetron 3), with oxygen as a reactive gas. The bipolar co-sputtering process enables the fine-tuning of the film composition by varying sputtering pulse lengths. For this upper layer, the deposition parameters are shown in Table 3.

Table 3. Deposition parameters of (Ti,Si)O₂ thin films and their EDX analysis.

Sample	Temperature	Si Pulse-on	Setpoint	O ₂ Flow ¹	Total Pressure	Thickness	Rate	Ti	Si	O
No.	°C	μs	%	sccm	Pa	nm	nm/m	at. %	at. %	at. %
TiSiO_1	250	5	10	29	1.09	1289	43	32.6	1.2	66.2
TiSiO_2	250	6	10	23	1.09	955	32	26.3	8.2	65.5
TiSiO_3	250	7	10	21	1.09	988	33	22.1	12.6	65.3
TiSiO_4	250	8	10	28	1.09	1041	35	17.4	17.5	65.1
TiSiO_5	250	6	15	20	1.10	610	20	11.9	22.9	65.2
TiSiO_6	250	6	25	22	1.17	402	13	6.6	28.2	65.2

¹ Average value taken during the deposition process.

2.2. Characterization

Cross-sections of the layers and layer stacks were prepared using a broad ion beam preparation technique (Cross Section Polisher, SM-0910, Jeol, Peabody, MA, USA), and the microstructure of these cross sections was investigated by high-resolution field emission scanning electron microscopy (FE-SEM, SU 8000, Hitachi, Tokyo, Japan); for this purpose, the crystal orientation or channeling contrast and the material contrast of backscattered electrons were used. For chemical composition analysis, energy-dispersive X-ray spectroscopy (EDX, EDAX Octane Elect system, Pleasanton, CA, USA) measurements were carried out at an acceleration voltage of 10 kV. Depth profiles of the layer composition were determined by RF glow-discharge optical emission spectrometry (GD OES, GD Profiler 2, Horiba Jobin Yvon, Kyoto, Japan). The structure of the obtained films was analyzed by X-ray diffraction (XRD, D8 Discover, Bruker, Billerica, MA, USA) using Cu-K α radiation and symmetric parallel beam arrangement, as well as grazing incidence diffraction. The spectral transmittance and reflectance of the films on borosilicate glass substrates were measured with a LAMBDA 19 UV-Vis-NIR spectrophotometer (Perkin Elmer, Waltham, MA, USA) using hemispherical transmission and reflection in the wavelength range from 300 nm to 2000 nm. Electrical conductivities of the deposited tungsten films were calculated from the sheet resistance obtained from four-point probe measurements at 20 °C.

The apparent water contact angle (WCA) was measured using a contact angle goniometer (Data Physics OCA 20, Filderstadt, Germany) and the sessile drop method after thin-film deposition. Measurements were carried out using 0.5 μ L deionized water droplets at room temperature (20–22 °C) and five measurements were performed for each sample at different positions of the thin-film surface for statistical purposes. Afterwards, the samples were stored in the dark under ambient conditions and the WCA was periodically mea-

sured using the previously mentioned procedure to study the effects of natural aging on the film wettability. Additionally, surface free energies were calculated using the Owens–Wendt–Rabel–Kaelble (OWRK) method, by measuring the contact angles of deionized water, diiodomethane, and ethylene glycol on the thin films.

3. Results and Discussion

3.1. Tungsten Top Electrodes

Tungsten exhibits a high thermal (bulk: 170 W/m·K at 20 °C) and electrical conductivity (bulk: 18.5 MS/m) [22]. The measured electrical conductivity values of the W coatings are listed in Table 1 and range between 3.1 and 4.1 MS/m, corresponding to 17%–22% of the bulk value. This allows them to be used as the outer or top electrodes of the electrocaloric components. Moreover, tungsten is chemically and mechanically stable, leading to a better bonding of the WO₃ layer to the ceramic substrate.

As shown in Figure 2, the four samples exhibit a columnar nanocrystalline microstructure with porosity at the grain boundaries. The lateral grain size of the layers is in the range of 200 to 350 nm. The films deposited at a higher pulse frequency (W_2 and W_4) seem to have a more disturbed microstructure, which also explains their lower electrical conductivity. The deposition parameters 500 °C and 2.5 kHz of sample W_3 have been chosen for further experiments as they lead to a microstructure with pores at the grain boundaries through the whole layer, needed for the complete wetting application according to Equation (2). Furthermore, this sample shows, in channeling contrast, a microstructure with fewer lattice defects due to the reduction in ion energy caused by the low sputter voltage and by the high substrate temperature [23].

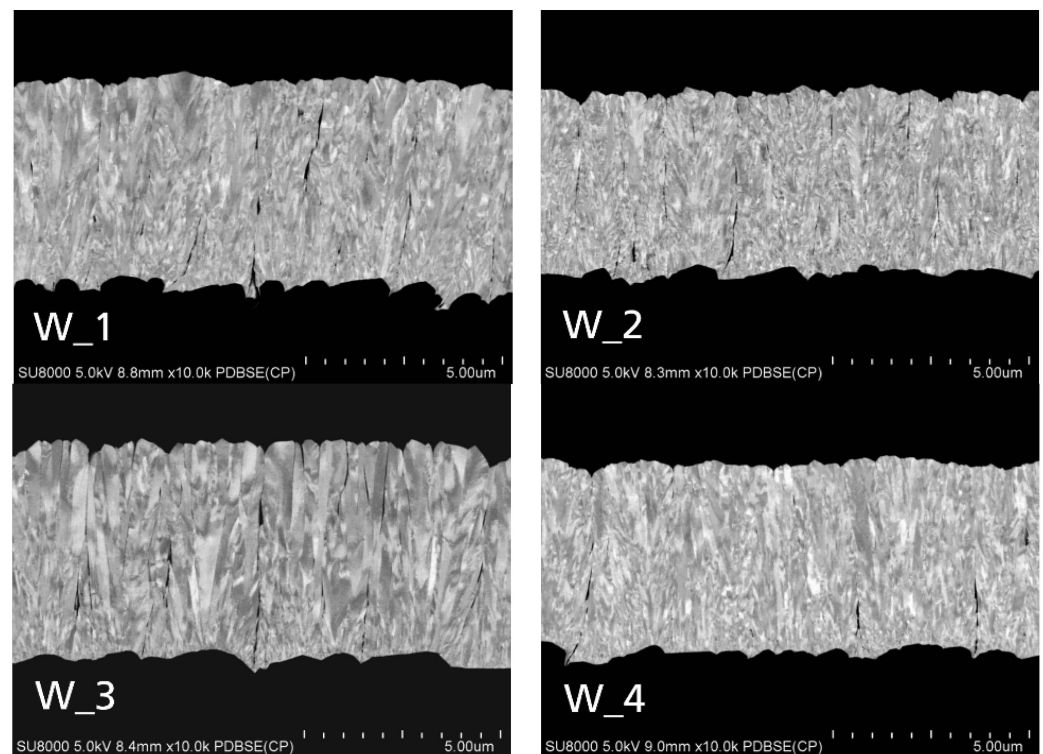


Figure 2. FE-SEM cross-section micrographs of the magnetron-sputtered W films deposited on Al₂O₃ ceramic substrates.

Figure 3 shows the XRD pattern of the chosen sample, which corresponds to the diffractogram of the bcc (α -W) crystal structure with a statistic crystal orientation distribution. The International Centre for Diffraction Data (ICDD) #04-0806 has been used to evaluate the crystal phase. Moreover, the measured static water contact angle of the as-deposited W film had a value of 5° and increased to 56° after one month of dark storage.

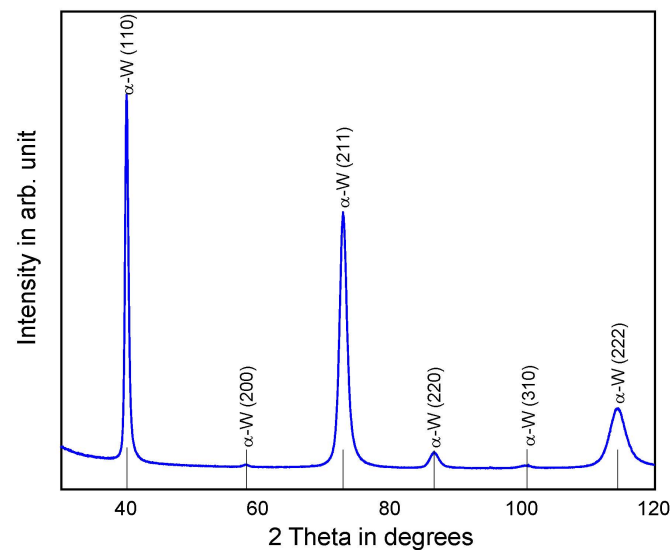


Figure 3. X-ray diffractogram of the W film deposited at 500 °C, using a pulse frequency of 2.5 kHz.

3.2. Tungsten Trioxide Thin Films

As mentioned before, the composition and oxygen vacancies of tungsten oxides determine their band gap and therefore their light absorption properties. Hence, for this material system, the first step was to adjust the setpoint for controlling the oxygen gas flow to obtain the desired composition and stoichiometry of the coatings required for the superhydrophilic application. For this purpose, several samples were produced with a variation in the setpoint (see the first three samples in Table 2). The visual appearance of these samples deposited on Al_2O_3 ceramic substrates is presented in Figure 4 and a significant color difference among them can be appreciated. The film with a setpoint of 70% (left) has a dark appearance, indicating that the tungsten is still in a metallic state and has not been completely oxidized yet. The film with a setpoint of 90% (middle) exhibits a violet color, typical of non-stoichiometric tungsten oxide (WO_{3-x}), while the film deposited at a setpoint of 130% has a yellow appearance, which is the characteristic color of WO_3 [24,25]. Moreover, for the setpoint of 130%, a stoichiometric WO_3 composition was determined by EDX analysis.



Figure 4. Visual appearance of 2 μm thick WO_x films on Al_2O_3 ceramic substrates, deposited at different setpoint values for controlling the inlet flow of O_2 into the vacuum chamber. From left to right: 70% (WO_{x_1}), 90% (WO_{x_2}), and 130% (WO_{x_3}).

SEM surface micrographs, ion-polished cross-section images, and GD-OES profiles of samples WO_{x_1} , WO_{x_2} , and WO_{x_3} are presented in Figure 5. A nanocrystalline structure can be observed for the three different films, where the crystallite size tends to increase with a higher (more reactive) setpoint. Additionally, there is a visible change in the material contrast in the cross-section image of the film deposited at a setpoint of 70% (Figure 5d), indicating a change in the stoichiometry in the direction of the layer growth, which can

also be validated from the fluctuation in the GD-OES profile (Figure 5g). This effect can be explained by an instability of process control of the reactive mode of magnetron sputtering. On the other hand, the sample deposited at a setpoint of 130% (WO_{x_3}) exhibits a slightly rougher surface with slightly bigger crystallites of 100 nm and a columnar structure. For this sample, a lower deposition rate is also noticeable, which led to a thinner coating.

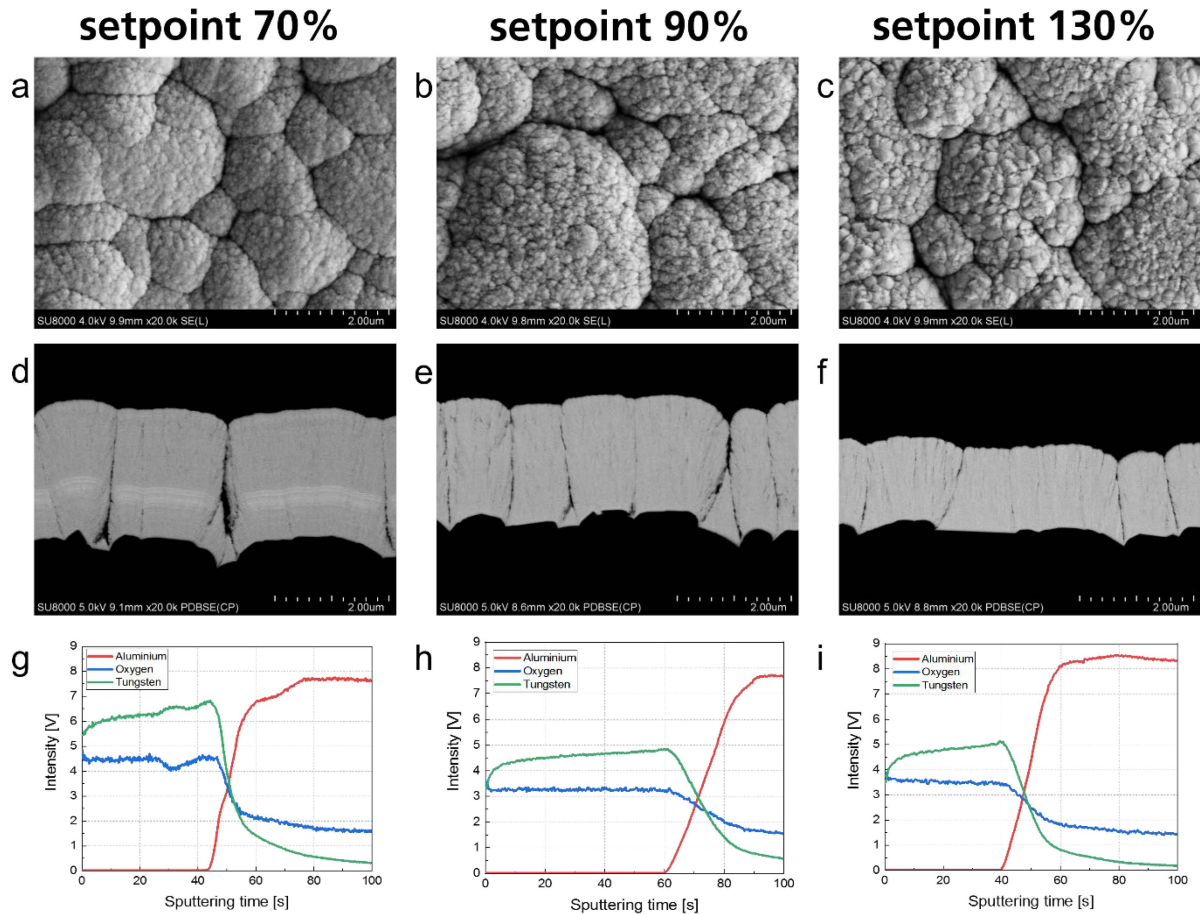


Figure 5. FE-SEM surface micrographs (a–c), ion-polished cross-section micrographs (d–f), and GD-OES intensity—sputtering time profiles (g–i) of 2 μm thick WO_x films on Al_2O_3 ceramic substrates, deposited at different setpoint values for controlling the inlet flow of O_2 into the vacuum chamber. From left to right: 70% (WO_{x_1}), 90% (WO_{x_2}), and 130% (WO_{x_3}).

In terms of wettability, the three films exhibit a hydrophilic behavior. However, as can be observed in Figure 6, only the samples deposited with higher setpoints (90% and 130%) show superhydrophilicity as deposited. Furthermore, after 28 days of dark storage, the WCA of the films deposited with a setpoint of 70% and 90% increases from 31° to 49° and from 6° to 10° , respectively, while the sample deposited with a setpoint of 130% still exhibits a complete wetting behavior with a WCA of 0° . Compared to the other two samples, the higher and longer-lasting wettability of sample WO_{x_3} can be attributed to its larger surface area due to surface roughness; moreover, there might be some additional effects caused by the higher chemical sorption of water molecules, as described by Colovic et al. [26]. Since the film deposited at a setpoint of 130% exhibits chemical stability, a rough microstructure, and perfect wetting behavior even after 28 days of dark storage, this setpoint has been chosen as the standard parameter for the next film depositions.

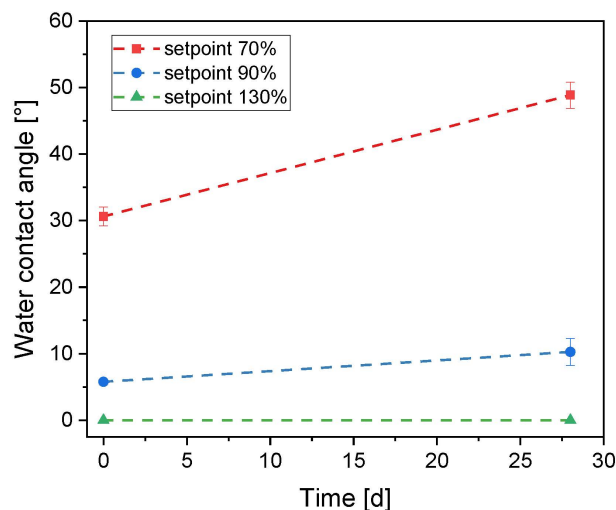


Figure 6. Static WCA of 2 μm thick WO_x films on Al_2O_3 ceramic substrates, deposited at different setpoint values for controlling the inlet flow of O_2 into the vacuum chamber. The measurement was carried out right after film deposition (day 0) and again after 28 days of dark storage under ambient conditions.

Having established the optimal setpoint for O_2 flow into the vacuum chamber, the influences of deposition temperature and film thickness on the wetting properties were also considered. Figure 7 shows the FE-SEM cross-section micrographs of samples WO_3_4 (deposited at 250 $^\circ\text{C}$) and WO_3_5 (deposited at 500 $^\circ\text{C}$) and their respective X-ray diffractograms. Both samples exhibit a lateral grain size of about 100 nm and deep grooves caused by the large grain size of the Al_2O_3 ceramic substrate, which ranges between 1 and 2 μm ; however, the film deposited at 500 $^\circ\text{C}$ (Figure 7b) has a columnar microstructure with a relatively high porosity. In the XRD results, it is possible to observe that the sample deposited at 250 $^\circ\text{C}$ exhibits a monoclinic (m- WO_3) phase with a preferred orientation along the (002) plane, while the one deposited at 500 $^\circ\text{C}$ shows diffractions corresponding to the orthorhombic (o- WO_3) crystal phase and a preferred orientation along the (200) and (020) planes. The International Centre for Diffraction Data (ICDD) #71-1465 and #71-0131 have been used to evaluate the crystal phases. The difference in morphology between the two samples can thus be attributed to the two different crystal phases formed. Moreover, the higher porosity of the film deposited at 500 $^\circ\text{C}$ can be related to the increased mobility of the deposited atoms at higher substrate temperatures, which triggers this type of columnar growth [27,28].

In order to evaluate the influence of deposition temperature and film thickness on surface wettability, tungsten trioxide coatings were deposited at 250 $^\circ\text{C}$ and 500 $^\circ\text{C}$ and the deposition time was varied to obtain films with thicknesses between 50 nm and 1 μm . The evolution of the static WCA for a period of 120 days after deposition is shown in Figure 8; day 0 corresponds to the day on which the films were synthesized. The films deposited at 500 $^\circ\text{C}$ with an orthorhombic structure exhibit better wettability, i.e., lower contact angles than the ones deposited at 250 $^\circ\text{C}$ with a monoclinic structure. This can be explained by the increased surface roughness and porosity of the films deposited at a higher temperature, which provide a larger contact surface for the spreading liquid. On the other hand, for both deposition temperatures, the thicker films show a more hydrophilic behavior due to the deeper grooves that promote water spreading owing to capillary action. Furthermore, the 1 μm thick WO_3 film deposited at 500 $^\circ\text{C}$ exhibits superhydrophilic properties even after 120 days of dark storage.

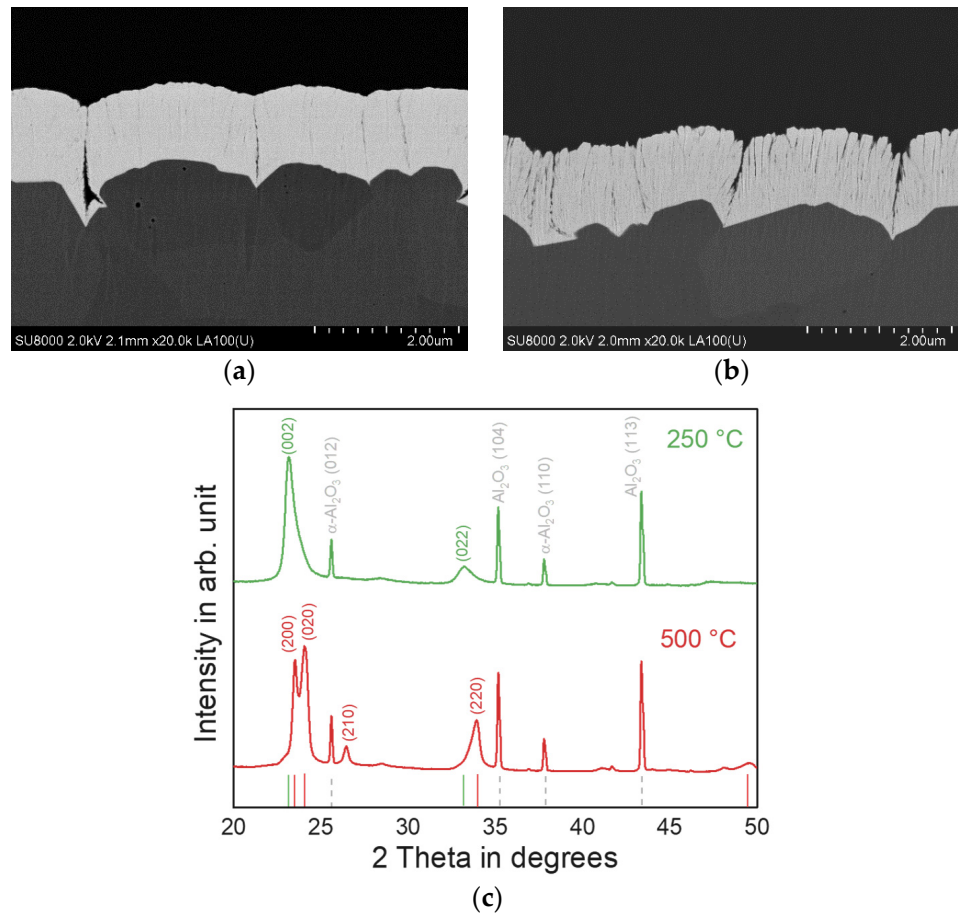


Figure 7. FE-SEM cross-section micrographs of 1 μm WO_3 coatings deposited at 250 °C (a) and 500 °C (b), and their respective X-ray diffractograms (c).

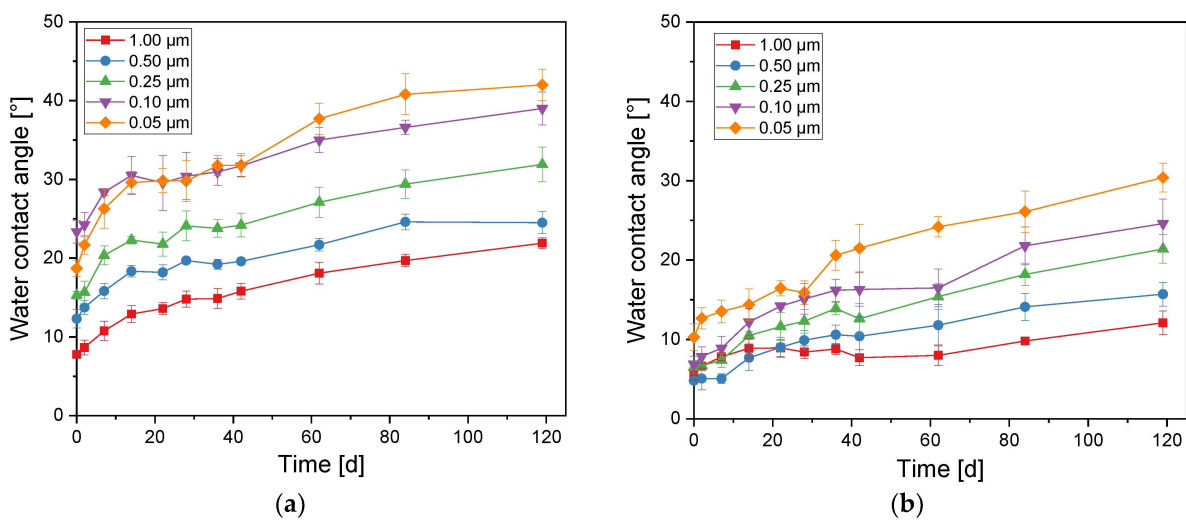


Figure 8. Evolution of the static water contact angle of WO_3 coatings deposited at 250 °C (a) and 500 °C (b) on Al_2O_3 ceramic substrates with a variation in thickness. After each measuring point, the samples were stored in the dark until the next measurement.

Due to the higher porosity and improved wetting behavior of the films deposited at 500 °C, this temperature was selected as the optimum temperature for producing hydrophilic tungsten trioxide coatings. The influence of film thickness on the optical properties of the WO_3 films was investigated by UV-Vis-NIR spectrophotometry and Figure 9a

shows their absorbance spectra. The absorption edge of the films is found in the range from 430 to 460 nm, with the smallest wavelength corresponding to the thickest film and the largest to the thinnest one. The indirect optical band gap, E_g , of the films was obtained by extrapolation to the abscissa of the plot of $(\alpha hv)^{1/2}$ against hv using the Tauc relation [29] from the transmittance spectra:

$$(\alpha hv)^{1/2} = C(hv - E_g) \quad (3)$$

where α is the absorption coefficient, hv is the incident photon energy, and C is a constant of proportionality, and the results are presented in Figure 9b. The band-gap values of the sputtered WO_3 films estimated by this method are 2.61, 2.67, 2.81, 2.84, and 2.85 eV for the thicknesses 1, 0.5, 0.25, 0.1, and 0.05 μm , respectively. These values are in accordance with the one reported in the literature for the bulk material, which is 2.7 eV [30,31]. The shift in the absorption edge towards higher wavelengths (lower photon energy) with increasing film thickness can be explained by the usual decrease in transmittance for thicker films.

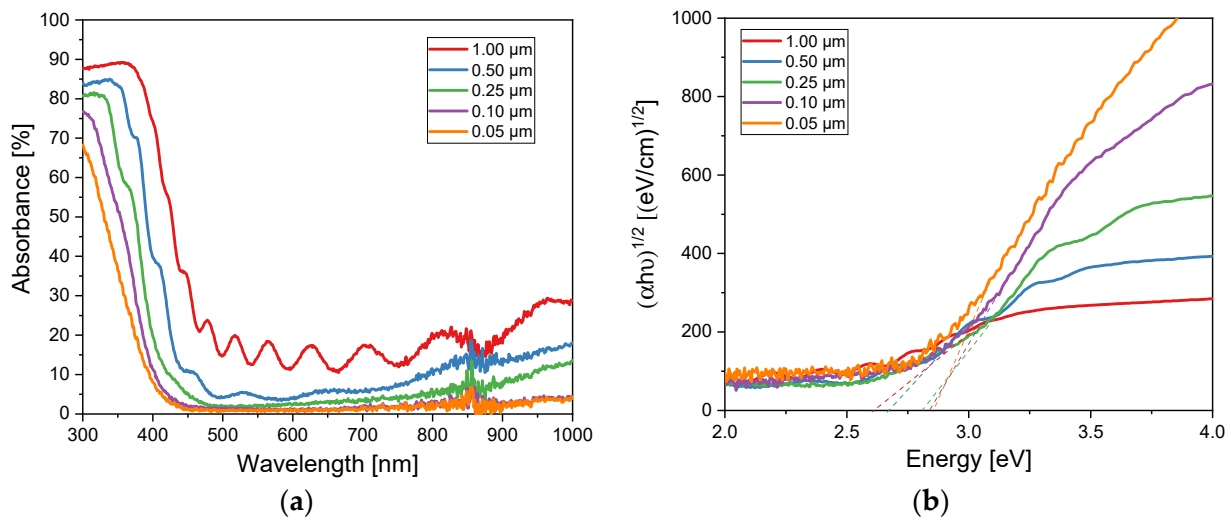


Figure 9. (a) Absorbance spectra of WO_3 coatings deposited at 500 $^\circ\text{C}$ on glass substrates with a variation in thickness. (b) Tauc plots of the same films.

Regarding optical properties, film thickness does not seem to be a critical factor, since the band gap energy values of all the films are in the range of the visible spectrum, which is desirable in the case of requiring a reactivation of the complete wetting performance of the films by visible light. However, thicker films exhibit a longer lasting superhydrophilicity, and thus a WO_3 film at least 1 μm thick deposited at 500 $^\circ\text{C}$ has been selected for further experiments.

3.3. Titanium Dioxide–Silicon Dioxide Outer Layer

The composition of the $(\text{Ti,Si})\text{O}_2$ films was adjusted by varying the silicon pulse-on time between 5 and 8 μs , while the titanium and silicon pulse-off times were kept constant at 10 μs , as well as the titanium pulse-on time, which was kept at 16 μs . The setpoint for controlling the oxygen gas flow into the vacuum chamber was also adjusted. The deposition parameters of the films, together with their respective EDX analysis, are shown in Table 3, and the SEM micrographs, as well as the X-ray diffractograms are presented in Figure 10.

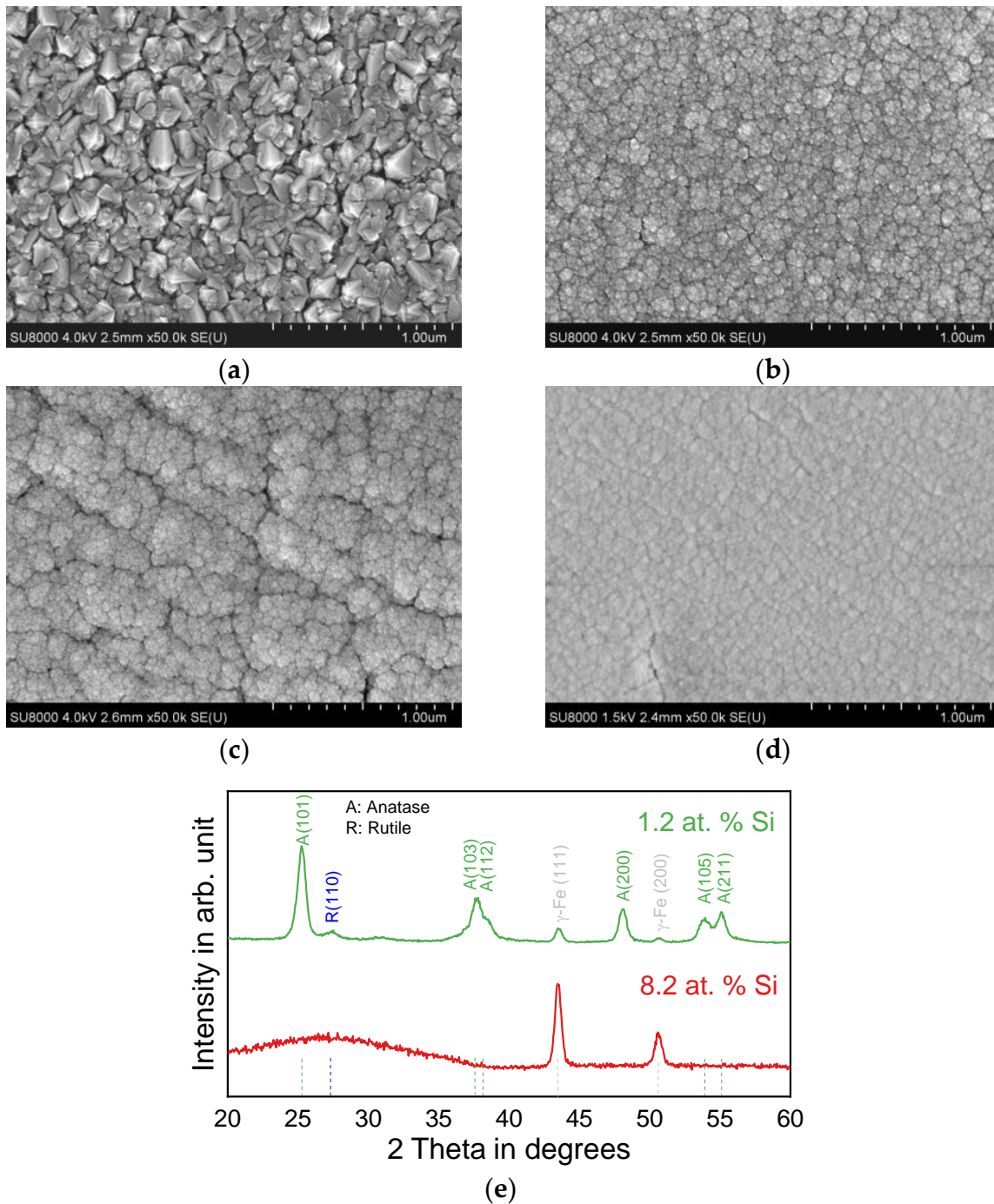


Figure 10. FE-SEM micrographs of 1 μm thick $(\text{Ti,Si})\text{O}_2$ coatings deposited on stainless-steel substrates at 250 $^\circ\text{C}$ with different compositions: 1.2 (a), 8.2 (b), 17.5 (c), and 28.2 (d) at. % Si; and grazing incidence (1°) X-ray diffractograms of the samples with 1.2 and 8.2 at. % Si (e).

As expected, longer Si pulse-on times lead to more Si-containing thin films. Increasing the setpoint for controlling the oxygen gas flow inlet produces silicon-rich films, which might be a consequence of the earlier onset of oxide coverage on the Ti target, resulting in a drastic reduction in its deposition rate. From the SEM micrographs, it can be observed that the film sputtered with a shorter Si pulse-on length (Figure 10a) exhibits a crystallite morphology typical of anatase TiO_2 . Moreover, as the silicon content increases, the films become amorphous, forming cauliflower-like clusters (Figure 10b–d). The X-ray diffractograms presented in Figure 10e show mainly the diffraction peaks of anatase TiO_2 and one

very weak rutile TiO_2 diffraction peak in the film with 1.2 at. % Si, while the film with 8.2 at. % Si exhibits a broad hump typical of amorphous materials. The International Centre for Diffraction Data (ICDD) #21-1272 and #21-1276 were used for this evaluation. The XRD results of the other samples with more Si content (not shown here) also exhibit amorphous patterns. This suppressive effect on the formation of crystalline anatase when adding SiO_2 has also been reported by Chien et al. [32].

The wetting properties of the sputtered $(\text{Ti,Si})\text{O}_2$ coatings are shown in Figure 11. In this case, the best surface wettability is observed in films with a silicon content between 12.6 and 22.9 at. %, in which a stable water contact angle of approximately 20° is reached on the fiftieth day after deposition and is kept constant even after 112 days of dark storage, demonstrating that the long-lasting hydrophilicity can be improved by a moderate increase in the silicon content. This enhanced wetting behavior is attributed to the formation of amorphous films with a mesoporous microstructure and increased surface area [15,16]. As observed in the SEM micrograph (Figure 10d), the sample with the highest silicon content has a smooth surface, which explains why its wettability drops and its contact angle increases to more than 30° after only 10 days of dark storage. Consequently, the sublayers produced for the superhydrophilic application were synthesized with a Si content between 12.6 and 22.9 at. %.

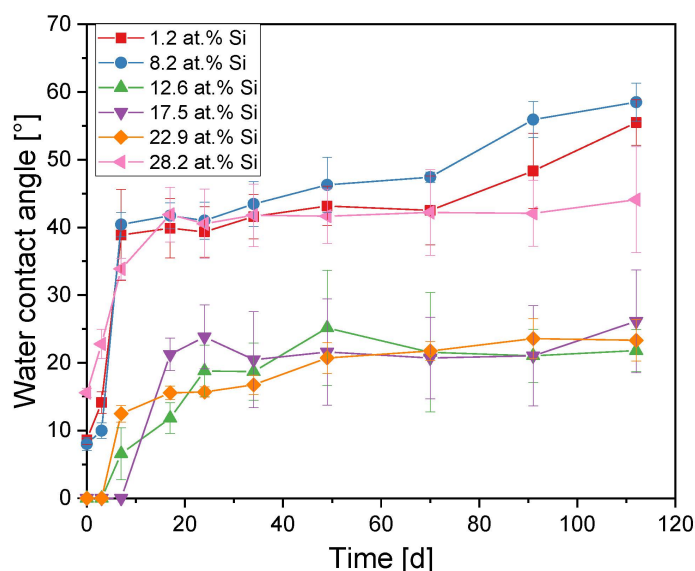


Figure 11. Evolution of the static water contact angle of $(\text{Ti,Si})\text{O}_2$ coatings deposited at 250°C on stainless steel substrates with variation in composition. Day 0 corresponds to the day on which the films were synthesized. After each measuring point, the samples were stored in the dark until the next measurement.

3.4. Multilayer System

The microstructure of a $(\text{Ti,Si})\text{O}_2/\text{WO}_3/\text{W}$ multilayer containing 17.5 at. % Si in the top layer is presented in Figure 12 and looks comparable to the microstructure of the two samples with a Si content of 12.6 and 22.9 at. % (not shown here). As it can be observed, due to the columnar growth, a mesoporous structure has been developed; it consists of intercolumnar porosity formed by deep grooves that go from the outer film surface to the grains of the ceramic substrate, accompanied by intermediate mesopores with diameters of less than 50 nm. Furthermore, the $(\text{Ti,Si})\text{O}_2$ outer layer exhibits the expected cauliflower-like surface structure with its characteristic nano-roughness.

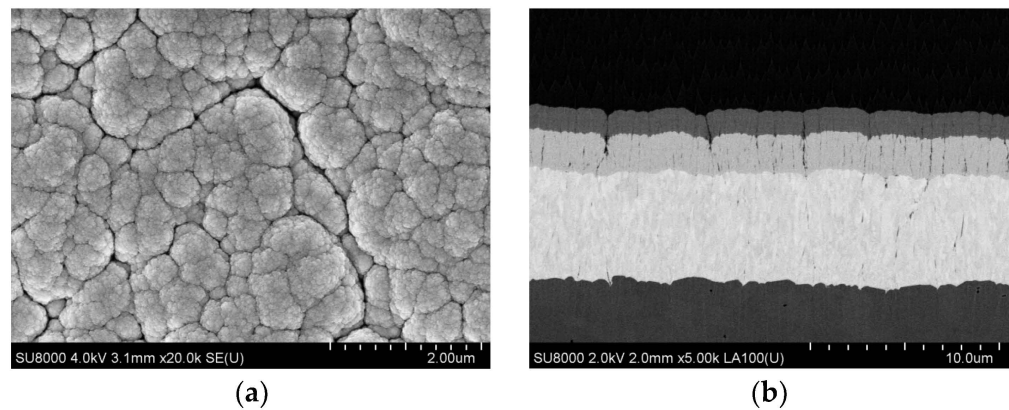


Figure 12. FE-SEM micrograph (a) and cross-section (b) of a magnetron sputtered long-lasting superhydrophilic multilayer consisting of 1 μm $(\text{Ti,Si})\text{O}_2$ /2 μm WO_3 /5 μm W deposited on Al_2O_3 ceramic substrate. The $(\text{Ti,Si})\text{O}_2$ film has a composition of 17.5 at. % Si.

Regarding wettability, the bare Al_2O_3 substrate shows a WCA of 57° , while the multilayered systems exhibit a superhydrophilic behavior for more than seven months of dark storage (Figure 13a), independently of the silicon content. The decrease in water contact angle of the samples after being exposed to daylight for 3 h on the 75th day demonstrates the feasibility of visible light reactivation of the coatings thanks to the presence of the tungsten trioxide film. Moreover, as observed in Figure 13b, the apparent surface energy of the Al_2O_3 ceramic substrates increases from 42.0 to 68.6 mN/m when coating them with the layer stack; in this case, both the polar and dispersive components of the free energy increase, leading to stronger interactions between the solid surface and the water molecules, thus improving the wetting properties.

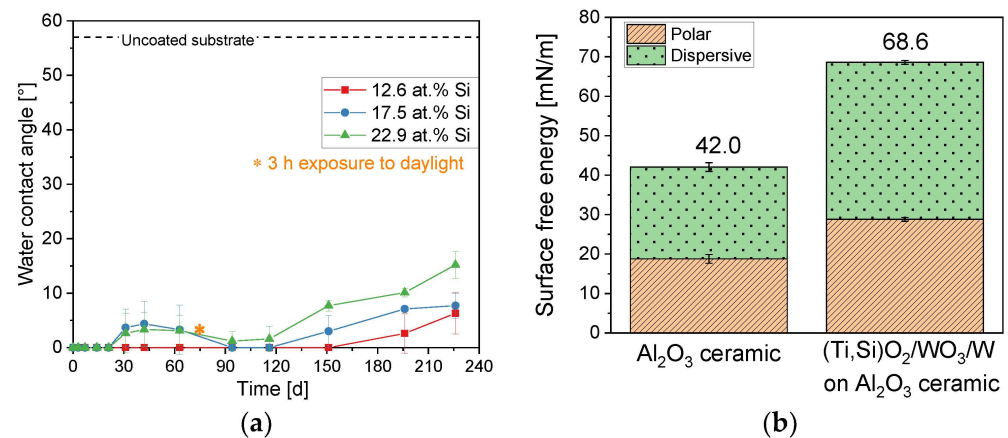


Figure 13. (a) Static water contact angle evolution during several months of dark storage of $(\text{Ti,Si})\text{O}_2/\text{WO}_3/\text{W}$ multilayers deposited on Al_2O_3 ceramic substrates with variation in the silicon content of the outer film. On day 75, the films were exposed to daylight for 3 h. (b) Surface energy of an Al_2O_3 ceramic substrate with its polar and dispersive components before and after coating it with the $(\text{Ti,Si})\text{O}_2/\text{WO}_3/\text{W}$ multilayer.

Static water contact angle measurements denote a reliable and easily accessible method for characterizing the wettability of the coatings; however, for the specific application of surface functionalization in cooling devices, where not only a complete wetting of the surface by a fluid is intended, but also fast wetting and dewetting processes are required, additional assessment techniques are necessary. For this purpose, the contact line dynamics of 0.5 μL water drops evaporating on uncoated and coated Al_2O_3 ceramic substrates at room temperature have been analyzed and the results are presented in Figure 14.

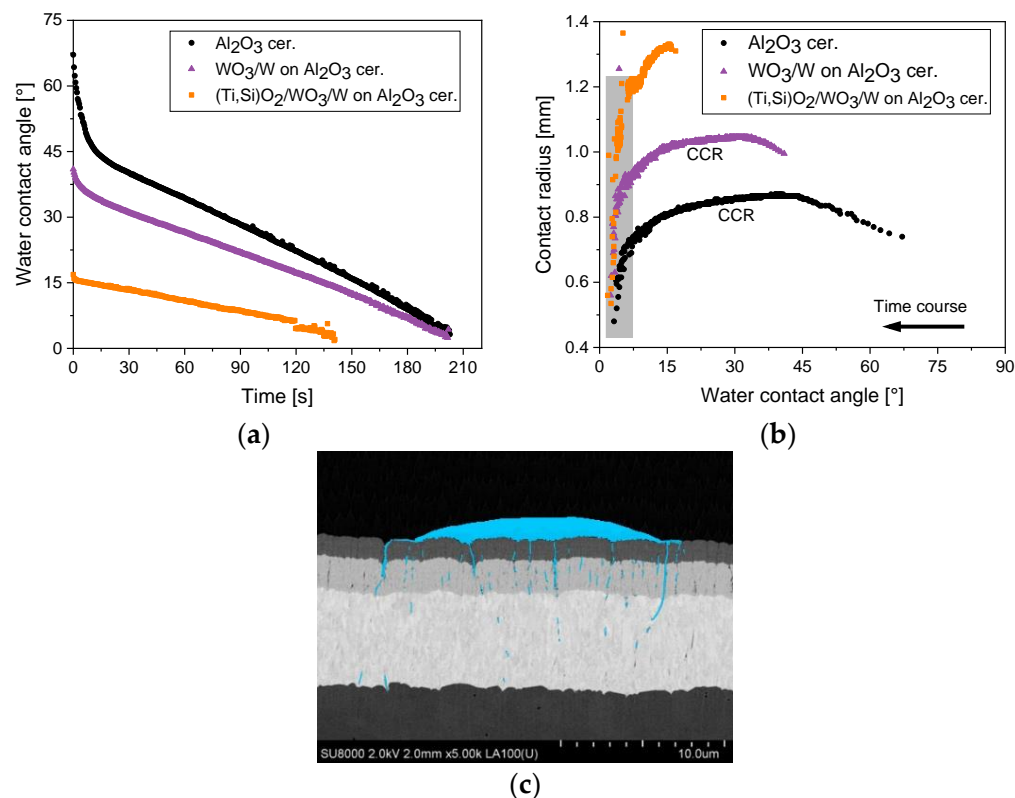


Figure 14. Evolution of contact angle over time (a) and contact line dynamics (b) during the evaporation of a 0.5 μL water drop on uncoated and coated Al_2O_3 ceramic substrates at room temperature. For the contact line dynamics, the grey area represents the CCA mode. Schematic representation of the spreading and wicking processes on the synthesized superhydrophilic coatings at the nanometric scale (c).

As can be perceived in Figure 14a, although the sample coated with the bilayer WO_3/W exhibits a lower initial contact angle ($\text{WCA}_0 = 40^\circ$) than the bare Al_2O_3 ceramic substrate ($\text{WCA}_0 = 64^\circ$), the complete water drop evaporation takes 203 s on both samples. On the other hand, the substrate coated with the multilayer $(\text{Ti,Si})\text{O}_2/\text{WO}_3/\text{W}$ has an initial contact angle of 16° , which is 75% smaller than the one of the uncoated substrate, and the complete fading of the drop takes only 140 s, representing a reduction of 30% in the evaporation time compared to the other two samples. Additionally, the water drop placed on the multilayer also exhibits a larger contact radius during the evaporation process (Figure 14b), which means that the fluid wets a bigger area of the solid surface.

During the evaporation process of a droplet, two main modes of contact line dynamics are observed, which are referred to as constant contact radius (CCR) and constant contact angle (CCA). In the former, the contact radius remains constant with time, while in the second mode, the contact angle remains constant. Additionally, there is an intermediate or mixed mode, which is frequently observed as well [33,34]. In Figure 14b, the water drops on the bare substrate as well as on the substrate coated with the bilayer WO_3/W start evaporating in the CCR mode, which is followed by a short mixed stage and finally a brief CCA mode. Contrarywise, on the superhydrophilic layer stack, a CCA mechanism is observed for most of the evaporation time and the base radius decreases linearly.

The motion of a drop over a thin, porous layer is influenced by two competing processes: (i) the imbibition of the liquid from the deposited drop into the porous surface; and (ii) the spreading of the drop over parts of the surface that are already saturated with the liquid, which results in the expansion of the contact radius [35]. In this case, since the thickness of the films is much smaller than the drop height and given that the characteristic length of the droplet (its radius) is smaller than the capillary length of water, which is

2.71 mm at room temperature [36], gravity forces can be neglected, and capillary forces are assumed to be dominant.

Assuming a circular cross-section of the pores, the capillary pressure, p_c , inside the porous films can be estimated from the Young–Laplace equation:

$$p_c = \frac{2\gamma_{lv}}{a} \quad (4)$$

where a is the capillary radius inside the porous layers and γ_{lv} is the liquid–vapor interfacial tension. Additionally, the capillary pressure inside the drop, Δp , can be defined as

$$\Delta p = \frac{\gamma_{lv} H}{r^2} = \frac{\gamma_{lv} H}{r} \frac{1}{r} \quad (5)$$

where H is the drop height and r is the drop base radius [35]. In the case of hydrophilic surfaces, the low contact angle formed by the drop on the solid surface implies that $\frac{H}{r} \ll 1$, therefore $\frac{\gamma_{lv} H}{r} \ll \frac{\gamma_{lv}}{r} \ll \frac{\gamma_{lv}}{a}$, meaning that the capillary pressure inside the pores of the thin films is much higher than the capillary pressure inside the macroscopic drop itself. For this reason, the enhanced stability of superhydrophilicity can be attributed not only to the unique composition of the multilayered coatings, but also to the presence of abundant micro- and mesopores, which allow water to be drawn into the pores by capillary action, promoting wicking and spreading effects at the nanometric scale as represented schematically in Figure 14c, and thus leading to a perfect wetting performance of the films.

4. Conclusions

In this work, (Ti,Si)O₂/WO₃/W coatings have been synthesized by pulse magnetron sputtering. Deposition parameters such as substrate temperature, pulse times, pulse frequency, oxygen flow in the reactive processes, and deposition time have been optimized for each layer of the stack with the aim of tailoring their roughness, porosity, crystal structure, chemical stability, thickness, surface energy, optical properties, and composition in order to achieve long-term superhydrophilicity. It is worth mentioning that all the coatings examined in this work exhibit a very good adhesion strength, since during sample preparation for SEM analysis, there was no sign of delamination.

It has been found that the optimal silicon content of the (Ti,Si)O₂ outer layer ranges between 12.6 and 22.9 at. %, given that less or more silicon lowers the hydrophilicity. Additionally, since the estimated band gap energy values of the sputtered WO₃ films vary between 2.61 and 2.85 eV depending on their thickness, a reactivation of the complete wetting performance of the films by visible light should be feasible.

Regarding the wetting performance, the (Ti,Si)O₂/WO₃/W multilayers exhibit a superhydrophilic behavior for more than 220 days of dark storage, and an increase in apparent surface energy from 42.0 to 68.6 mN/m has been measured after coating Al₂O₃ ceramic substrates with these material systems. Moreover, contact line dynamics of 0.5 μL water drops show a reduction of 30% in the evaporation time on the Al₂O₃ ceramic substrates coated with the (Ti,Si)O₂/WO₃/W multilayer compared to the bare substrates. Additionally, water drops placed on the multilayer exhibit a constant contact angle mode of evaporation and larger contact radius during the evaporation process, meaning that the fluid wets a bigger area of the solid surface in contrast to the uncoated samples and the substrates coated only with the WO₃/W bilayer.

The enhanced wetting performance of the coatings is attributed not only to their intrinsic hydrophilic nature but also to the presence of abundant micro- and mesopores in their structure, which promote capillary action and the spreading of the liquid at the nanometric scale. Nevertheless, further investigations on the role of intermolecular bonding forces, disjoining pressures, and Laplace pressure inside the pores are needed to understand the wetting performance of the synthesized coatings at the nanometric length scale, which is beyond the scope of this work.

Finally, the sufficient electrical conductivity of 3.6 MS/m of the W underlayer, together with the long-term superhydrophilic performance of the (Ti,Si)O₂/WO₃ films that do not need a periodical reactivation, make these coatings suitable for use in solid-state cooling devices such as electrocaloric heat pumps or in applications in which a complete wetting of the surface by a fluid is required.

Author Contributions: Conceptualization, M.B. and F.F.; methodology, M.B. and F.F.; validation, F.F., O.Z. and T.M.; formal analysis, M.B.; investigation, M.B. and F.F.; data curation, M.B.; writing—original draft preparation, M.B.; writing—review and editing, F.F., O.Z. and T.M.; visualization, M.B.; supervision, F.F.; project administration, F.F.; funding acquisition, F.F. All authors have read and agreed to the published version of the manuscript.

Funding: This research was funded by Fraunhofer-Gesellschaft zur Förderung der angewandten Forschung e. V. as part of the lighthouse project “ElKaWe—Electrocaloric heat pumps”. Funding reference: 840 005. www.ElKaWe.org (accessed on 10 April 2024).

Institutional Review Board Statement: Not applicable.

Informed Consent Statement: Not applicable.

Data Availability Statement: Data are contained within the article.

Conflicts of Interest: The authors declare no conflicts of interest.

References

1. Mönch, S.; Reiner, R.; Waltereit, P.; Basler, M.; Quay, R.; Gebhardt, S.; Molin, C.; Bach, D.; Binninger, R.; Bartholomé, K. How highly efficient power electronics transfers high electrocaloric material performance to heat pump systems. *MRS Adv.* **2023**, *8*, 787–796. [[CrossRef](#)]
2. Zhu, S.; Xie, K.; Lin, Q.; Cao, R.; Qiu, F. Experimental determination of surface energy for high-energy surface: A review. *Adv. Colloid Interface Sci.* **2023**, *315*, 102905. [[CrossRef](#)] [[PubMed](#)]
3. Selvakumar, N.; Barschilia, H.C.; Rajam, K.S. Effect of substrate roughness on the apparent surface free energy of sputter deposited superhydrophobic polytetrafluoroethylene coatings: A comparison of experimental data with different theoretical models. *J. Appl. Phys.* **2010**, *108*, 013505. [[CrossRef](#)]
4. Young, T. An essay on the cohesion of fluids. *Philos. Trans. R. Soc. Lond.* **1805**, *95*, 65–87.
5. Ramana, C.V.; Battu, A.K.; Dubey, P.; Lopez, G.A. Phase-control-enabled enhancement in hydrophilicity and mechanical toughness in nanocrystalline tungsten oxide films for energy-related applications. *ACS Appl. Nano Mater.* **2020**, *3*, 3264–3274. [[CrossRef](#)]
6. Drelich, J.; Chibowski, E. Superhydrophilic and superwetting surfaces: Definition and mechanisms of control. *Langmuir* **2010**, *26*, 18621–18623. [[CrossRef](#)] [[PubMed](#)]
7. Azimirad, R.; Naseri, N.; Akhavan, O.; Moshfegh, A.Z. Hydrophilicity variation of WO₃ thin films with annealing temperature. *J. Phys. D Appl. Phys.* **2007**, *40*, 1134–1137. [[CrossRef](#)]
8. Miyauchi, M.; Nakajima, A.; Watanabe, A.; Hashimoto, K. Photocatalysis and photoinduced hydrophilicity of various metal oxide thin films. *Chem. Mater.* **2002**, *14*, 2812–2816. [[CrossRef](#)]
9. Kong, X.; Hu, Y.; Wang, X.; Pan, W. Effect of surface morphology on wettability conversion. *J. Adv. Ceram.* **2016**, *5*, 284–290. [[CrossRef](#)]
10. Vrakatseli, V.E.; Kalarakis, A.N.; Kalampounias, A.G.; Amanatides, E.K.; Mataras, D.S. Glancing angle deposition effect on structure and light-induced wettability of RF-sputtered TiO₂ thin films. *Micromachines* **2018**, *9*, 389. [[CrossRef](#)]
11. Frach, P.; Glöß, D.; Metzner, C.; Modes, T.; Scheffel, B.; Zywitzki, O. Deposition of photocatalytic TiO₂ layers by pulse magnetron sputtering and by plasma-activated evaporation. *Vacuum* **2006**, *80*, 679–683. [[CrossRef](#)]
12. Fateh, R.; Dillert, R.; Bahnemann, D. Preparation and characterization of transparent hydrophilic photocatalytic TiO₂/SiO₂ thin films on polycarbonate. *Langmuir* **2013**, *29*, 3730–3739. [[CrossRef](#)]
13. Adachi, T.; Latthe, S.S.; Gosavi, S.W.; Roy, N.; Suzuki, N.; Ikari, H.; Kato, K.; Katsumata, K.-I.; Nakata, K.; Furudate, M.; et al. Photocatalytic, superhydrophilic, self-cleaning TiO₂ coating on cheap, light-weight, flexible polycarbonate substrates. *Appl. Surf. Sci.* **2018**, *458*, 917–923. [[CrossRef](#)]
14. Yao, L.; He, J. Facile dip-coating approach to fabrication of mechanically robust hybrid thin films with high transmittance and durable superhydrophilicity. *J. Mater. Chem. A* **2014**, *2*, 6994–7003. [[CrossRef](#)]
15. Bai, Z.; Hu, Y.; Yan, S.; Shan, W.; Wei, C. Preparation of mesoporous SiO₂/Bi₂O₃/TiO₂ superhydrophilic thin films and their surface self-cleaning properties. *RSC Adv.* **2017**, *7*, 1966–1974. [[CrossRef](#)]
16. Chen, P.; Hu, Y.; Wei, C. Preparation of superhydrophilic mesoporous SiO₂ thin films. *Appl. Surf. Sci.* **2012**, *258*, 4334–4338. [[CrossRef](#)]

17. Hendi, A.; Al-Kuhaili, M.; Durrani, S.M.A.; Faiz, M.; Ul-Hamid, A.; Qurashi, A.; Khan, I. Modulation of the band gap of tungsten oxide thin films through mixing with cadmium telluride towards photovoltaic applications. *Mater. Res. Bull.* **2017**, *87*, 148–154. [[CrossRef](#)]
18. Zhang, M.; Yang, C.; Zhang, Z.; Tian, W.; Hui, B.; Zhang, J.; Zhang, K. Tungsten oxide polymorphs and their multifunctional applications. *Adv. Colloid Interface Sci.* **2022**, *300*, 102596. [[CrossRef](#)]
19. Bandi, S.; Srivastav, A. Review: Oxygen-deficient tungsten oxides. *J. Mater. Sci.* **2021**, *56*, 6615–6644. [[CrossRef](#)]
20. Zhang, R.; Ning, F.; Xu, S.; Zhou, L.; Shao, M.; Wei, M. Oxygen vacancy engineering of WO₃ toward largely enhanced photoelectrochemical water splitting. *Electrochim. Acta* **2018**, *274*, 217–223. [[CrossRef](#)]
21. Schiller, S.; Goedicke, K.; Reschke, J.; Kirchhoff, V.; Schneider, S.; Milde, F. Pulsed magnetron sputtering technology. *Surf. Coat. Technol.* **1993**, *61*, 331–337. [[CrossRef](#)]
22. Billings, B.H.; Gray, D.E. *American Institute of Physics Handbook*, 3rd ed.; McGraw-Hill: New York, NY, USA, 1972.
23. Ellmer, K. Magnetron sputtering of transparent conductive zinc oxide: Relation between the sputtering parameters and the electronic properties. *J. Phys. D Appl. Phys.* **2000**, *33*, R17. [[CrossRef](#)]
24. Weil, M.; Schubert, W.-D. *The Beautiful Colors of Tungsten Oxides*; International Tungsten Industry Association: London, UK, 2013.
25. Guillen, C. Polycrystalline WO_{3-x} thin films obtained by reactive DC sputtering at room temperature. *Materials* **2023**, *16*, 1359. [[CrossRef](#)] [[PubMed](#)]
26. Colovic, B.; Kistic, D.; Jokanovic, B.; Rakocevic, Z.; Nasov, I.; Petroska, A.; Jokanovic, V. Wetting properties of titanium oxides, oxynitrides and nitrides obtained by DC and pulsed magnetron sputtering and cathodic arc evaporation. *Mater. Sci.-Pol.* **2019**, *37*, 173–181. [[CrossRef](#)]
27. Xia, Z.-J.; Wang, H.-L.; Su, Y.-F.; Tang, P.; Dai, M.-J.; Lin, H.-J.; Zhang, Z.-G.; Shi, Q. Enhanced electrochromic properties by improvement of crystallinity for sputtered WO₃ film. *Coatings* **2020**, *10*, 577. [[CrossRef](#)]
28. Gullapalli, S.K.; Vemuri, R.S.; Manciu, F.S.; Enriquez, J.L.; Ramana, C.V. Tungsten oxide (WO₃) thin films for application in advanced energy systems. *J. Vac. Sci. Technol. A* **2010**, *28*, 824–828. [[CrossRef](#)]
29. Tauc, J.; Grigorovici, R.; Vancu, A. Optical properties and electronic structure of amorphous Germanium. *Physica Status Solidi* **1966**, *15*, 627–637. [[CrossRef](#)]
30. Zhao, Y.; Balasubramanyam, S.; Sinha, R.; Lavrijsen, R.; Verheijen, M.A.; Bol, A.A.; Bieberle-Hütter, A. Physical and chemical defects in WO₃ thin films and their impact on photoelectrochemical water splitting. *ACS Appl. Energy Mater.* **2018**, *1*, 5887–5895. [[CrossRef](#)]
31. Subrahmanyam, A.; Karuppasamy, A. Optical and electrochromic properties of oxygen sputtered tungsten oxide (WO₃) thin films. *Sol. Energy Mater. Sol. Cells* **2007**, *91*, 266–274. [[CrossRef](#)]
32. Chien, D.M.; Viet, N.N.; Van, N.T.K.; Phong, N.T.P. Characteristics modification of TiO₂ thin films by doping with silica and alumina for self-cleaning application. *J. Exp. Nanosci.* **2009**, *4*, 221–232. [[CrossRef](#)]
33. Golovko, D.S.; Butt, H.-J.; Bonaccorso, E. Transition in the evaporation kinetics of water microdrops on hydrophilic surfaces. *Langmuir* **2008**, *25*, 75–78. [[CrossRef](#)] [[PubMed](#)]
34. Lopes, M.C.; Bonaccorso, E. Evaporation control of sessile water drops by soft viscoelastic surfaces. *Soft Matter* **2012**, *8*, 7875–7881. [[CrossRef](#)]
35. Starov, V.M.; Kostvintsev, S.R.; Sobolev, V.D.; Velarde, M.G.; Zhdanov, S.A. Spreading of liquid drops over dry porous layers: Complete wetting case. *J. Colloid Interface Sci.* **2002**, *252*, 397–408. [[CrossRef](#)]
36. Günay, A.A.; Kim, M.-K.; Yan, X.; Miljkovic, N.; Sett, S. Droplet evaporation dynamics on microstructured biphilic, hydrophobic, and smooth surfaces. *Exp. Fluids* **2021**, *62*, 153. [[CrossRef](#)]

Disclaimer/Publisher’s Note: The statements, opinions and data contained in all publications are solely those of the individual author(s) and contributor(s) and not of MDPI and/or the editor(s). MDPI and/or the editor(s) disclaim responsibility for any injury to people or property resulting from any ideas, methods, instructions or products referred to in the content.